

Supplement of Atmos. Chem. Phys., 18, 14017–14036, 2018  
<https://doi.org/10.5194/acp-18-14017-2018-supplement>  
© Author(s) 2018. This work is distributed under  
the Creative Commons Attribution 4.0 License.



*Supplement of*

## **Molecular and physical characteristics of aerosol at a remote free troposphere site: implications for atmospheric aging**

**Simeon K. Schum et al.**

*Correspondence to:* Lynn R. Mazzoleni (lrmazzol@mtu.edu)

The copyright of individual parts of the supplement might differ from the CC BY 4.0 License.

## Table of Contents

Description	Page
Pico Mountain Observatory	2
Supplemental Methods: OC/EC, IC	2
Supplemental Methods: IC, FLEXPART, QA	3
Supplemental Methods: SPE effect estimation	4
Supplemental Methods: SPE effect estimation results	5-6
Table S1, ESI instrumentation parameters	6
Table S2, Number of common species	6
Table S3, Molecular formula composition average values	7
Table S4, Literature BrC formula comparison	7
Table S5, Dry glass transition temperatures	8
Table S6, Atmospheric water comparison	8
Figure S1, PMO-1 FLEXPART results	9
Figure S2, PMO-2 FLEXPART results	10
Figure S3 PMO-3 FLEXPART results	11
Figure S4, FLEXPART carbon monoxide source apportionment	12
Figure S5, Wildfire emissions from GFAS dataset	13
Figure S6, Reconstructed mass spectra	14
Figure S7, Violin plots of O/C values	15
Figure S8, Violin plots of OS <sub>C</sub> values	15
Figure S9, Common and unique formulas histograms	16
Figure S10, Comparison of PMO-1 and PMO-2 unique CHOS	17
Figure S11, H/C and DBE histograms	18
Figure S12, Aethalometer observations	19
Figure S13, OS <sub>C</sub> vs. volatility from Donahue et al. (2011)	20
Figure S14, OS <sub>C</sub> vs. volatility from Li et al. (2016)	20
Figure S15, Correlation of Donahue method vs. Li method	21
Figure S16, Violin plots of dry T <sub>g</sub> values	21
Figure S17, Estimated T <sub>g</sub> distributions with mean RH	22
Figure S18, Estimation of T <sub>g</sub> estimation error boxplot	23
Figure S19, Cloud water composition comparison	23
Figure S20, OM and ion concentrations	24
Figure S21, van Krevelen plots for all species separated by elemental group and sample	25
Figure S22, Reconstructed mass spectra of PMO-2	26
Figure S23, Difference mass spectra	27
Equations S1-S7	28-29
References	30

## Pico Mountain Observatory

Pico Mountain Observatory (PMO) is located in the summit caldera of Pico Mountain on Pico Island, in the Azores, Portugal (38.47 °N, 28.40 °W). The sampling site is located at an altitude of 2225 m asl. Pico Mountain is the highest mountain in Portugal and in the central North Atlantic region (Honrath et al., 2008). The sampling site is often in the free troposphere as the marine boundary layer height in the area is normally between 500 and 2000 m (Kleissl et al., 2007; Rémillard et al., 2012; Zhang et al., 2017). At the site there is a variety of instrumentation such as a seven wavelength aethalometer, a nephelometer, an optical particle counter, and an ozone detector. In various studies this site has been denoted as PMO, PICO-NARE, and OMP. Its identifying code is PIC in the NOAA database.

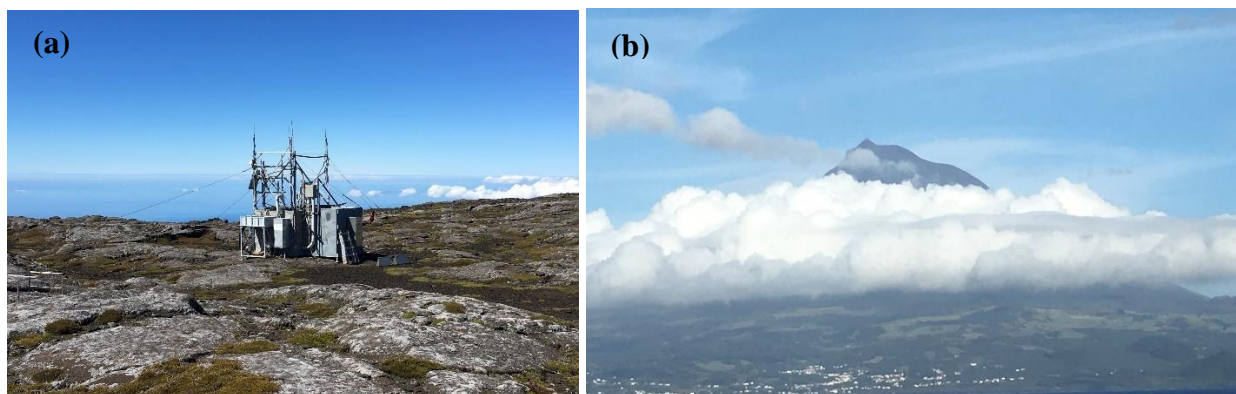


**Image 1.** Photos of the research station on the summit caldera of Pico Mountain (a) and Pico Mountain from neighboring Faial Island with the mountain summit above the cloud layer (b).

## Organic and elemental carbon analysis

For each sample collected, a minimum of three circular 16 mm diameter filter punches were analyzed. If all three punches had consistent organic carbon concentrations (relative standard deviation, RSD < 15 %), the average value was used to determine the total loading of OC on the filter and in the air during the sampling period. If the replicates were inconsistent, more replicates were analyzed until at least three were consistent. Elemental carbon measurements were also obtained with this instrument, but in nearly all cases they were below the detection limit, so those values are not reported.

## Ion chromatography

PMO samples were also analyzed for major anions and cations using ion chromatography (IC). Anion analysis was performed using a Dionex ICS-2100 instrument (Thermo Scientific) with an AS-17-C analytical and guard column set (Thermo Scientific) using a KOH generator for gradient elution. The gradient elution had the following steps: -5 – 0 min., Equilibrate, 1 mM KOH, 0 – 15 min., Isocratic, 1 mM KOH, 15 – 20 min., Ramp, 1 – 10 mM KOH, 20 – 30 min., Isocratic, 10 mM KOH, 30 – 40 min., Ramp, 10 – 20 mM KOH, 40 – 45 min., Isocratic, 20 mM KOH, 45 – 55 min., and Ramp, 20 – 40 mM KOH.

Cation analysis was performed using a Dionex ICS-1100 instrument with CS-12A analytical and guard column set (Thermo Scientific) and an isocratic 20 mM methanesulfonic acid eluent. The instruments were operated in parallel using split flow from autosampler. The samples were prepared using the California Air Resource Board method (California Environmental Protection Agency, 2011). Briefly, five square punches of 3.98 cm<sup>2</sup> each were taken from each filter and placed into a pre-cleaned 15 mL disposable centrifuge tube, to which 100 µL of isopropanol was added to help dissolve the less soluble organic species. Finally, 12 mL of 18.2 MOhm deionized water from an Easy Pure water system (Barnstead, ThermoFisher Waltham, MA, USA) were added to each centrifuge tube. These samples were then sonicated for 60 minutes with blue ice added to the sonication bath to keep the temperature below 25 °C. Once sonicated, the samples were stored in the refrigerator overnight and transferred with 0.45 µm nylon syringe filters (Fisher Brand, Waltham, MA, USA) and sterile 3 mL syringes (BD, Franklin Lakes, NJ, USA) to 5 mL IC vials (Thermo Scientific, Waltham, MA, USA) the following day. The samples were then run on the IC system. After the ion concentrations were determined, they were background subtracted using field blanks from PMO.

### **FLEXPART retroplume analysis**

Retroplume analysis was conducted using the Lagrangian particle dispersion model FLEXPART. (Seibert and Frank, 2004; Stohl et al., 2005; Owen and Honrath, 2009) The backward mode of FLEXPART was used to simulate backward transport trajectories from the PMO. The Global Forecast System (GFS) fields were used to drive FLEXPART. In the backward mode, hundreds of thousands of passive particles (tracer) were released from the receptor. The advection and dispersion of the particles were simulated backwards in time. The product of a backward simulation is an upwind spatial distribution of the particle residence times (average time an air parcel stays within a model grid cell), referred to as a “retroplume” (Seibert and Frank, 2004). In this study we report three specific events, one that took place on June 27 (19:00) -28 (19:00), 2013 (PMO-1), one on July 05 (15:00) - 06 (15:00), 2014 (PMO-2), and one on June 20 (15:00) - 21 (15:00), 2015 (PMO-3).

### **Ultrahigh resolution FT-ICR mass spectrometry quality assurance**

The quality assurance (QA) was performed to eliminate improbable molecular formulas and possible contaminants for each of the ultrahigh resolution FT-ICR mass spectra consistent with previous studies from our group (Putman et al. 2012; Mazzoleni et al. 2012; Dzepina et al. 2015). First, molecular formulas with extremely high or low O/C (>2, <0.1), H/C (>2.2, <0.3), and DBE (>20) are removed. All of the known solvent contaminant peaks and isolated assignments that are not associated with a CH<sub>2</sub> homologous series are removed. Blank subtraction was done by finding the ratio of intensities between a sample and a blank and then formulas with intensities < 3x larger than in the blank are removed or

flagged. After this is done, replicate analyses of the samples are evaluated and only the formulas that are present in both replicates are retained. If a formula is described as “not present” it means that formula was not present in the sample after the QA steps described here were performed.

### **Estimation of the SPE sample prep effect on the total WSOC properties**

As mentioned in the main paper, the solid phase extraction of WSOC results in the loss of some low molecular weight (MW) polar organic species and some high MW nonpolar species. Since the low molecular weight species are studied using ion chromatography, the major ions and their concentrations are known. Specifically, oxalate, formate, and acetate which are the most abundant can cause an underprediction of the average O/C value and an overprediction of average  $T_g$  values for a sample. In an effort to constrain the potential impact of this effect on our results, we used the concentrations of 5 organic acids detected by ion chromatography, along with their O/C values, and Boyer-Kauzmann rule ( $T_g = g \cdot T_m$ ,  $g = 0.7$ ) (Shiraiwa et al., 2017; DeRieux et al., 2018) estimated  $T_g$  values to estimate the weighted and unweighted average O/C and  $T_g$  values for the three samples if the organic acids were included.

To estimate the contribution of each organic anion to the overall organic mass, the mass concentrations were normalized by the organic mass (OM) concentration. The organic mass concentration was estimated by multiplying the measured OC concentration by 2, consistent with El-Zanan et al. (2005). The mass fractions were then multiplied by the sum of the total ion abundance in the mass spectrometry data (using assumption that they made up 50, 70, or 100% of organic mass) in order to roughly determine the potential ion abundances relative to those that were studied after SPE. While the results of the negative mode ESI do not likely represent the entirety of all organic species in the aerosol extracts, the polar compounds expected in water extracts are best ionized by this method and are expected to make up the majority of species (< 70%; Samburova et al., 2013). The estimated relative abundance of the low MW anions was used in conjunction with their O/C and  $T_g$  values to calculate a new weighted average for all of the compounds available for each sample. Using this approximation, we found that the addition of these small compounds had a very minor impact on the  $T_g$  values because they decreased by < 2.5 % at most. The percentage increase of the O/C values for the three samples varied from 20 % for PMO-1 to 42% for PMO-2. The ion weighted O/C value for PMO-1 is 0.58, for PMO-2, 0.81, and for PMO-3 is 0.57. The results confirm our observation that PMO-2 has much higher average O/C than PMO-1 or PMO-3, and that PMO-1 and PMO-3 have low O/C, considering their transport time in comparison to other studies (Bougiatioti et al., 2014). Based on these results, we conclude that although the loss of some low MW compounds using SPE can cause an under or an over prediction of some values, the effect in the

case of the samples in this study is minimal and does not change the implications of our observations.

Tables SM1-SM5 contain the values described in this discussion.

**Table SM1.** The concentrations of the ions used for the estimation and the organic mass (OM) concentration. The values are in  $\mu\text{g}/\text{m}^3$  air.

<b>Ion</b>	<b>PMO-1</b>	<b>PMO-2</b>	<b>PMO-3</b>
<b>Formate</b>	0.0289 $\pm$ 0.0003	0.00438 $\pm$ 0.00007	0.0119 $\pm$ 0.0001
<b>Acetate</b>	0.0519 $\pm$ 0.0001	0.004587 $\pm$ 0.000005	0.0071 $\pm$ 0.0002
<b>Oxalate</b>	0.0938 $\pm$ 0.00070	0.0897 $\pm$ 0.00181	0.0522 $\pm$ 0.00002
<b>Malonate</b>	0.00605 $\pm$ 0.0003	0.00548 $\pm$ 0.0007	0.0045 $\pm$ 0.0003
<b>Lactate</b>	0.0292 $\pm$ 0.0004	0.0019 $\pm$ 0.0001	0.00467 $\pm$ 0.0001
<b>OM</b>	4.14 $\pm$ 0.04	0.956 $\pm$ 0.052	1.74 $\pm$ 0.20

**Table SM2.** The percent mass fraction of each ion.

<b>Ion</b>	<b>PMO-1</b>	<b>PMO-2</b>	<b>PMO-3</b>
<b>Formate</b>	0.698	0.458	0.684
<b>Acetate</b>	1.25	0.479	0.409
<b>Oxalate</b>	2.27	9.38	3.00
<b>Malonate</b>	0.146	0.573	0.259
<b>Lactate</b>	0.705	0.199	0.268

**Table SM3.** The estimated  $T_g$  values for the acid form of each ion as estimated using their melting points and the Boyer-Kauzmann rule with  $g = 0.7$ .

<b>Ion</b>	<b><math>T_g</math></b>
<b>Formate</b>	197.1
<b>Acetate</b>	202.83
<b>Oxalate</b>	324.21
<b>Malonate</b>	285.6
<b>Lactate</b>	202.79

**Table SM4.** Estimated average O/C values when the ions are considered. The table contains the results for 3 assumptions of the organic mass fraction represented by the FT-ICR MS identified species (100%, 70%, 50%). The numbers in parentheses show the percent change in average O/C from the O/C without ions considered.

<b>Sample</b>	<b>RA Weighted O/C without Ions (100%)</b>	<b>Ions and RA Weighted O/C (100%)</b>	<b>Ions and RA Weighted O/C (70%)</b>	<b>Ions and RA Weighted O/C (50%)</b>
<b>PMO-1</b>	0.48	0.53 (10.42%)	0.55 (14.58%)	0.58 (20.83%)
<b>PMO-2</b>	0.57	0.70 (22.81%)	0.75 (31.58%)	0.81 (42.11%)
<b>PMO-3</b>	0.45	0.52 (15.56%)	0.54 (20.00%)	0.57 (26.67%)

**Table SM5.** Estimated average  $T_g$  values when the ions are considered. The table contains the results for 3 assumptions of the organic mass fraction represented by the FT-ICR MS identified species (100%, 70%, 50%). The numbers in parentheses show the percent change in average  $T_g$  from the  $T_g$  without ions considered. All  $T_g$  values are in K.

Sample	RA Weighted $T_g$ without Ions (100%)	Ions and RA Weighted $T_g$ (100%)	Ions and RA Weighted $T_g$ (70%)	Ions and RA Weighted $T_g$ (50%)
PMO-1	328.75	324.38 (1.33%)	322.67 (1.85%)	320.51 (2.51%)
PMO-2	326.45	324.43 (0.619%)	323.71 (0.839%)	322.85 (1.10%)
PMO-3	326.88	324.41 (0.756%)	323.44 (1.05%)	322.22 (1.43%)

## Supplemental Tables

**Table S1.** The ionization parameters for negative mode ESI FT-ICR MS for each of the samples.

Sample	Spray Voltage (V)	Sheath Gas Flow ( $\mu\text{L}/\text{min}$ )	Source Temp ( $^{\circ}\text{C}$ )
PMO-1 Rep 1	3.40	5.0	275
PMO-1 Rep 2	3.15	5.0	275
PMO-2 Rep 1	3.25	4.5	275
PMO-2 Rep 2	3.25	4.5	275
PMO-3 Rep 1	3.15	4.5	275
PMO-3 Rep 2	3.15	4.5	275

**Table S2.** Number of common species between this study and previous studies at PMO (Dzepina et al., 2015) and SPL (Mazzoleni et al., 2012). The percentages indicate the percent of common species for the sample indicated by the row names.

	PMO-1	PMO-2	PMO-3	Dzepina 2015	Mazzoleni 2012
PMO-1	X	1697 (53.6%)	1633 (51.5%)	2730 (86.2%)	1951 (61.6%)
PMO-2	1697 (80.0%)	X	1253 (59.1%)	1585 (74.7%)	1661 (78.3%)
PMO-3	1633 (89.7%)	1253 (68.8%)	X	1704 (90.6%)	1429 (76.0%)

**Table S3.** Unweighted average values with standard deviation and the numbers for each elemental group.

Sample	Group	O/C	H/C	DBE	OSc	Number
PMO-1	All	0.47 ± 0.15	1.29 ± 0.32	8.28 ± 3.69	-0.47 ± 0.49	3168
PMO-2	All	0.55 ± 0.19	1.37 ± 0.27	6.61 ± 2.85	-0.42 ± 0.49	2121
PMO-3	All	0.46 ± 0.12	1.33 ± 0.27	7.83 ± 3.07	-0.51 ± 0.42	1820
PMO-1	CHO	0.46 ± 0.16	1.28 ± 0.32	8.16 ± 3.68	-0.36 ± 0.50	1848
PMO-2	CHO	0.51 ± 0.18	1.37 ± 0.28	6.59 ± 2.79	-0.36 ± 0.53	1281
PMO-3	CHO	0.45 ± 0.13	1.36 ± 0.28	7.34 ± 3.11	-0.46 ± 0.45	1183
PMO-1	CHNO	0.48 ± 0.12	1.21 ± 0.24	9.40 ± 3.08	-0.53 ± 0.34	1120
PMO-2	CHNO	0.58 ± 0.15	1.26 ± 0.18	8.03 ± 2.27	-0.42 ± 0.32	561
PMO-3	CHNO	0.48 ± 0.09	1.24 ± 0.19	9.08 ± 2.33	-0.55 ± 0.27	608
PMO-1	CHOS	0.50 ± 0.14	1.77 ± 0.19	3.04 ± 1.61	-1.16 ± 0.41	200
PMO-2	CHOS	0.67 ± 0.26	1.61 ± 0.25	3.89 ± 2.12	-0.72 ± 0.49	274
PMO-3	CHOS	0.41 ± 0.10	1.90 ± 0.21	1.72 ± 1.22	-1.47 ± 0.19	29

**Table S4.** Molecular formulas identified in brown carbon by Iinuma et al. 2010 and Lin et al. 2016.

Formula	Observed	Citation
C <sub>7</sub> H <sub>7</sub> NO <sub>4</sub>	Yes	Iinuma et al. 2010; Lin et al. 2016
C <sub>6</sub> H <sub>5</sub> NO <sub>3</sub>	Yes	Lin et al. 2016
C <sub>6</sub> H <sub>5</sub> NO <sub>4</sub>	Yes	Lin et al. 2016
C <sub>6</sub> H <sub>6</sub> N <sub>2</sub> O <sub>6</sub>	No	Lin et al. 2016
C <sub>6</sub> H <sub>4</sub> NO <sub>4</sub>	No	Lin et al. 2016
C <sub>10</sub> H <sub>9</sub> NO <sub>3</sub>	No	Lin et al. 2016
C <sub>8</sub> H <sub>7</sub> NO <sub>4</sub>	Yes	Lin et al. 2016
C <sub>8</sub> H <sub>7</sub> NO <sub>3</sub>	Yes	Lin et al. 2016
C <sub>9</sub> H <sub>7</sub> NO <sub>4</sub>	Yes	Lin et al. 2016
C <sub>10</sub> H <sub>7</sub> NO <sub>4</sub>	Yes	Lin et al. 2016
C <sub>8</sub> H <sub>8</sub> O <sub>3</sub>	Yes	Lin et al. 2016
C <sub>9</sub> H <sub>6</sub> O <sub>3</sub>	Yes	Lin et al. 2016
C <sub>10</sub> H <sub>8</sub> O <sub>4</sub>	Yes	Lin et al. 2016
C <sub>13</sub> H <sub>8</sub> O <sub>5</sub>	Yes	Lin et al. 2016
C <sub>13</sub> H <sub>8</sub> O <sub>6</sub>	Yes	Lin et al. 2016
C <sub>15</sub> H <sub>10</sub> O <sub>6</sub>	Yes	Lin et al. 2016
C <sub>16</sub> H <sub>12</sub> O <sub>6</sub>	Yes	Lin et al. 2016
C <sub>16</sub> H <sub>12</sub> O <sub>7</sub>	Yes	Lin et al. 2016
C <sub>17</sub> H <sub>14</sub> O <sub>8</sub>	Yes	Lin et al. 2016

**Table S5.** Estimated average dry  $T_g$  for the three samples. All values are in K.

	<b>PMO-1</b>	<b>PMO-2</b>	<b>PMO-3</b>
<b>Unweighted</b>	333.76	328.94	333.56

**Table S6.** Number of molecular formulas and their average O/C values (unweighted O/C and RA weighted O/C ( $O/C_w$ )) uniquely common between this study and ambient aqueous organic matter (Mazzoleni et al., 2010; Zhao et al., 2015; Cook et al., 2017). Uniquely common means that the formula is common between only one of the PMO samples and the aqueous organic matter sample. CW indicates cloud water, the numbers in parentheses are the percentage of total formulas.

<b>Sample</b>	<b># Common Formula</b>	<b>O/C</b>	<b>O/C<sub>w</sub></b>
<b>PMO and Fog (Mazzoleni et al., 2010)</b>			
PMO-1	202 (6.4%)	0.38	0.39
PMO-2	48 (2.3%)	0.5	0.55
PMO-3	11 (0.60%)	0.29	0.29
<b>PMO and CW (Cook et al., 2017)</b>			
PMO-1	2 (0.063%)	0.82	0.82
PMO-2	23 (1.1%)	0.8	0.81
PMO-3	1 (0.055%)	0.36	0.36
<b>PMO and CW (Zhao et al., 2015)</b>			
PMO-1	197 (6.2%)	0.42	0.42
PMO-2	70 (3.3%)	0.76	0.8
PMO-3	42 (2.3%)	0.38	0.38

## Supplemental Figures

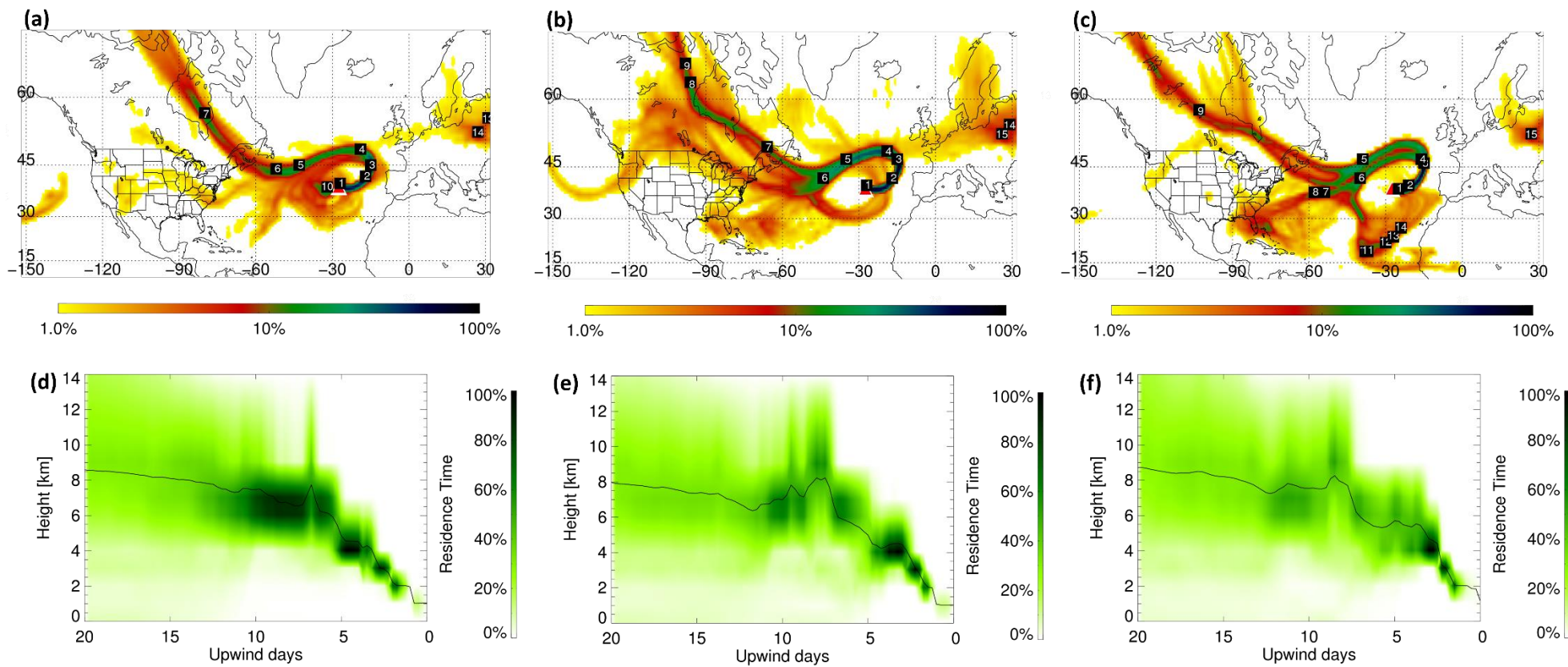


**Figure S1.** FLEXPART retroplumes the sampling period for PMO-1. June 27, 2013, 18:00 (a, d), June 28, 2013, 06:00 (b, e), and June 28, 2013, 18:00 (c, f).

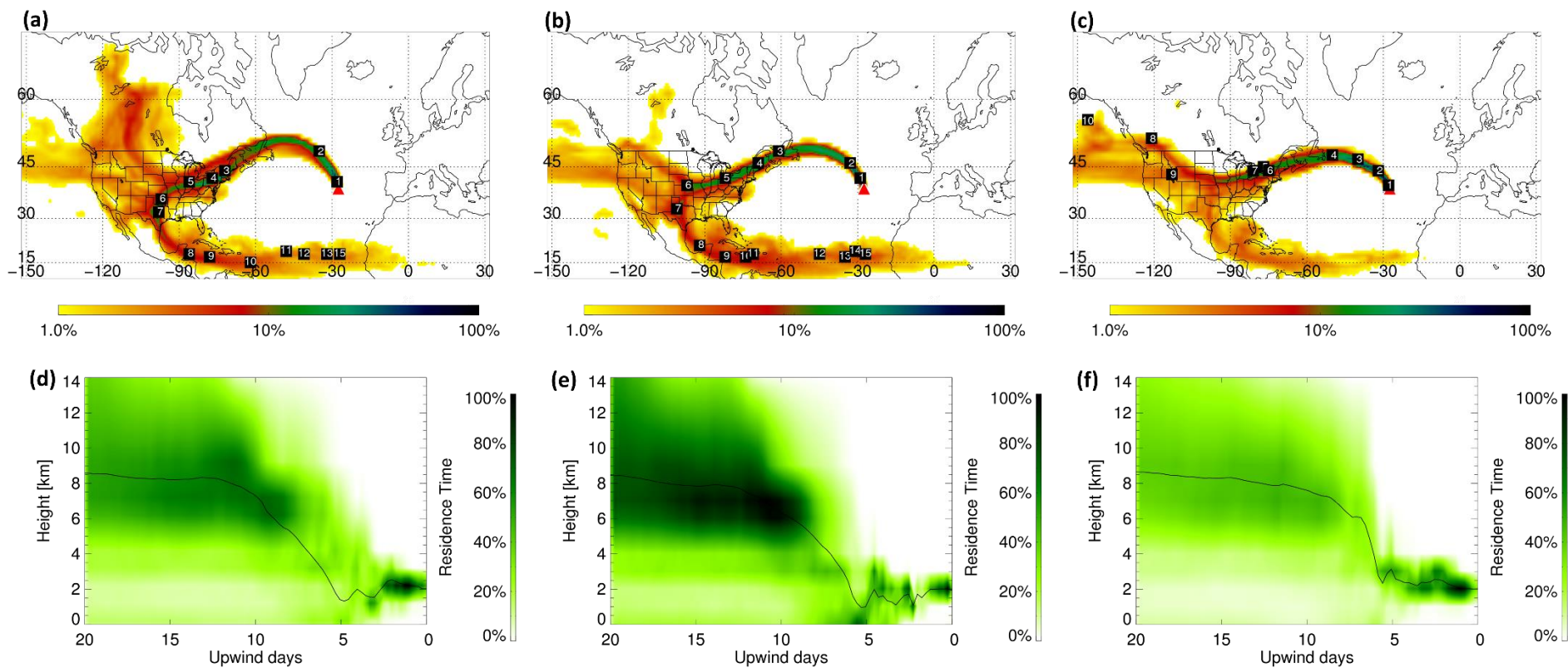


**Figure S2.** FLEXPART retrorplumes the sampling period for PMO-2. July 05, 2014, 15:00 (a, d), July 06, 2014, 03:00 (b, e), and July 06, 2014, 15:00 (c, f).

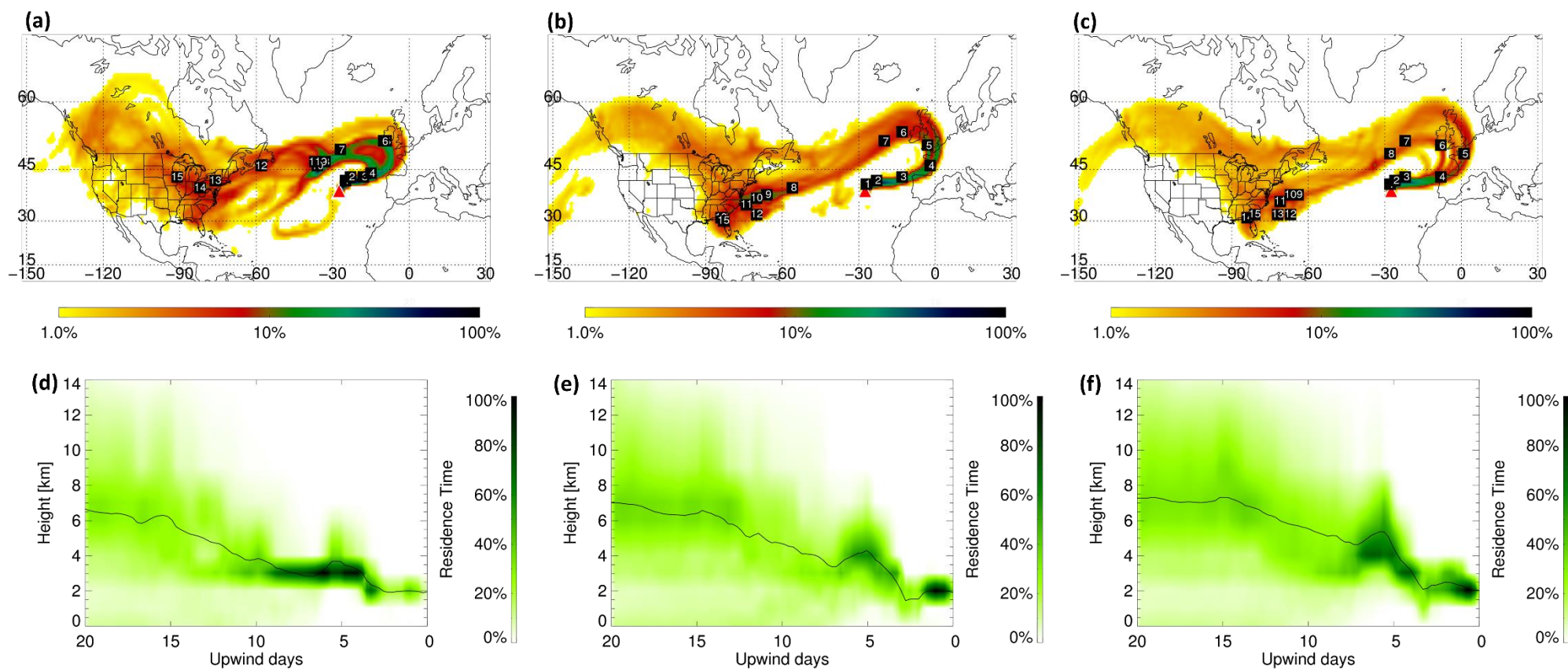


**Figure S3.** FLEXPART retroplumes the sampling period for PMO-3. June 20, 2015, 15:00 (a, d), June 21, 2015, 03:00 (b, e), and June 21, 2015, 15:00 (c, f).

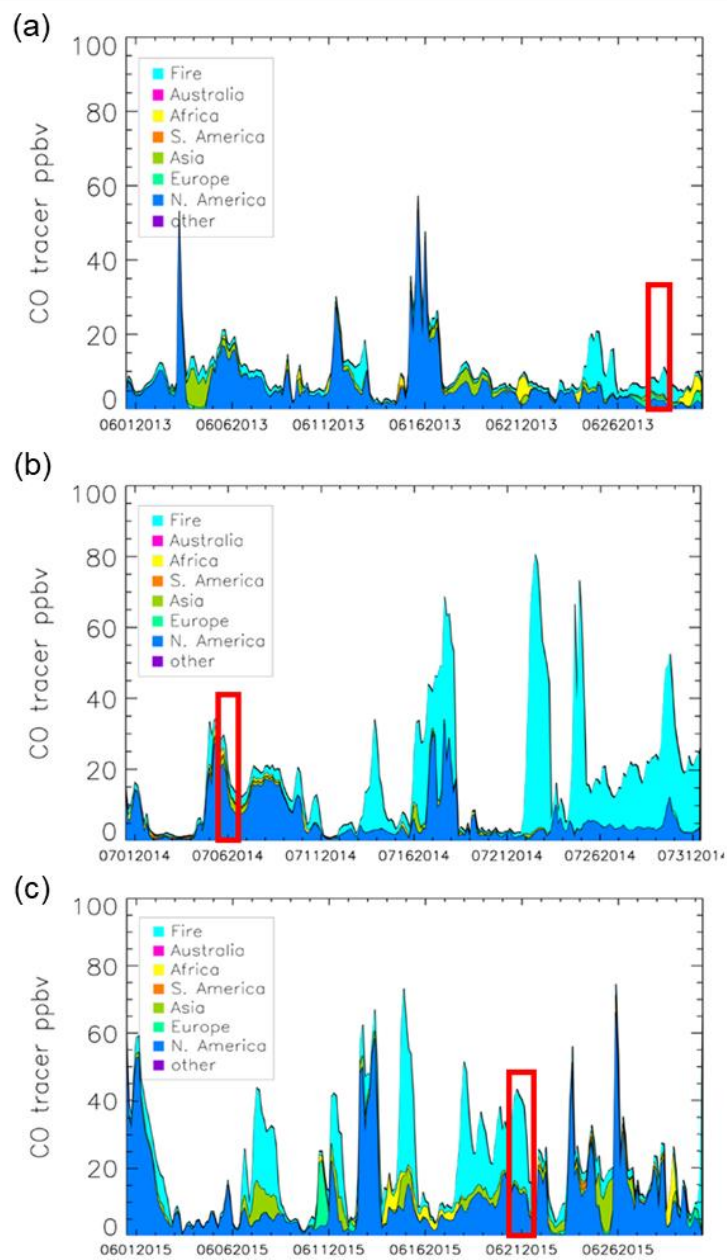


**Figure S4.** FLEXPART carbon monoxide source apportionment plot. PMO-1 (a), PMO-2 (b), PMO-3 (c). The red rectangle highlights the sampling period for each sample.

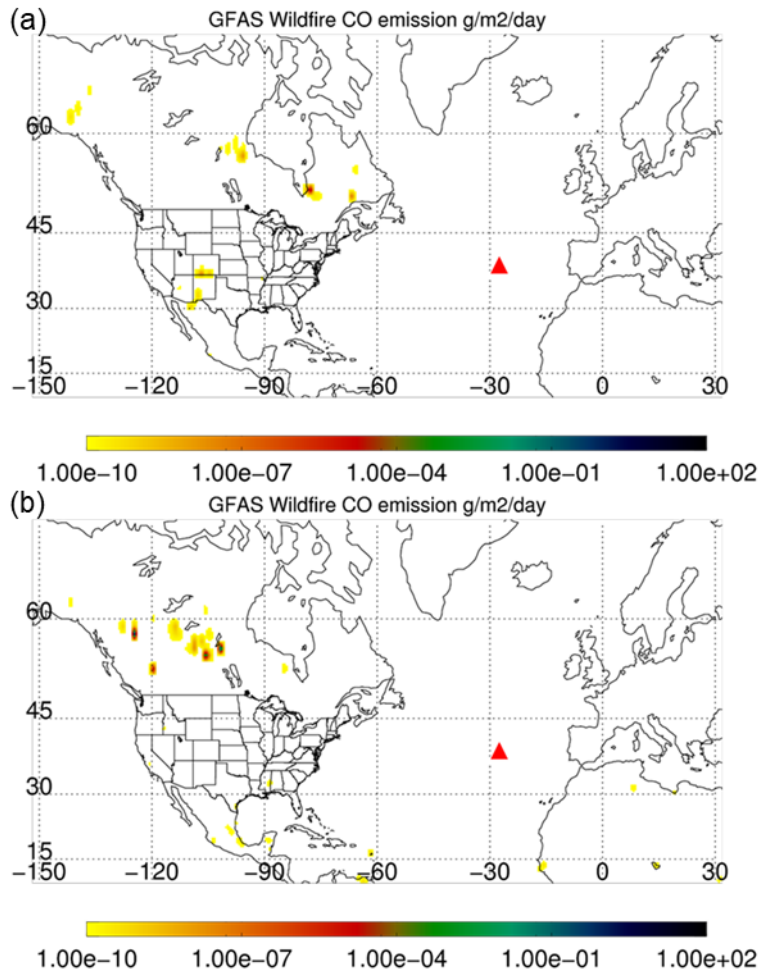


**Figure S5.** Wildfire emissions from GFAS dataset for the week corresponding to the PMO-1 event (a) and the PMO-3 event (b). Note the strong fire in western Quebec, which spatially coincides with the most likely path in the PMO-1 retroplume. Multiple fires in central and western Canada may have impacted PMO-3, although they are not spatially proximate to the most likely path in the PMO-3 retroplume.

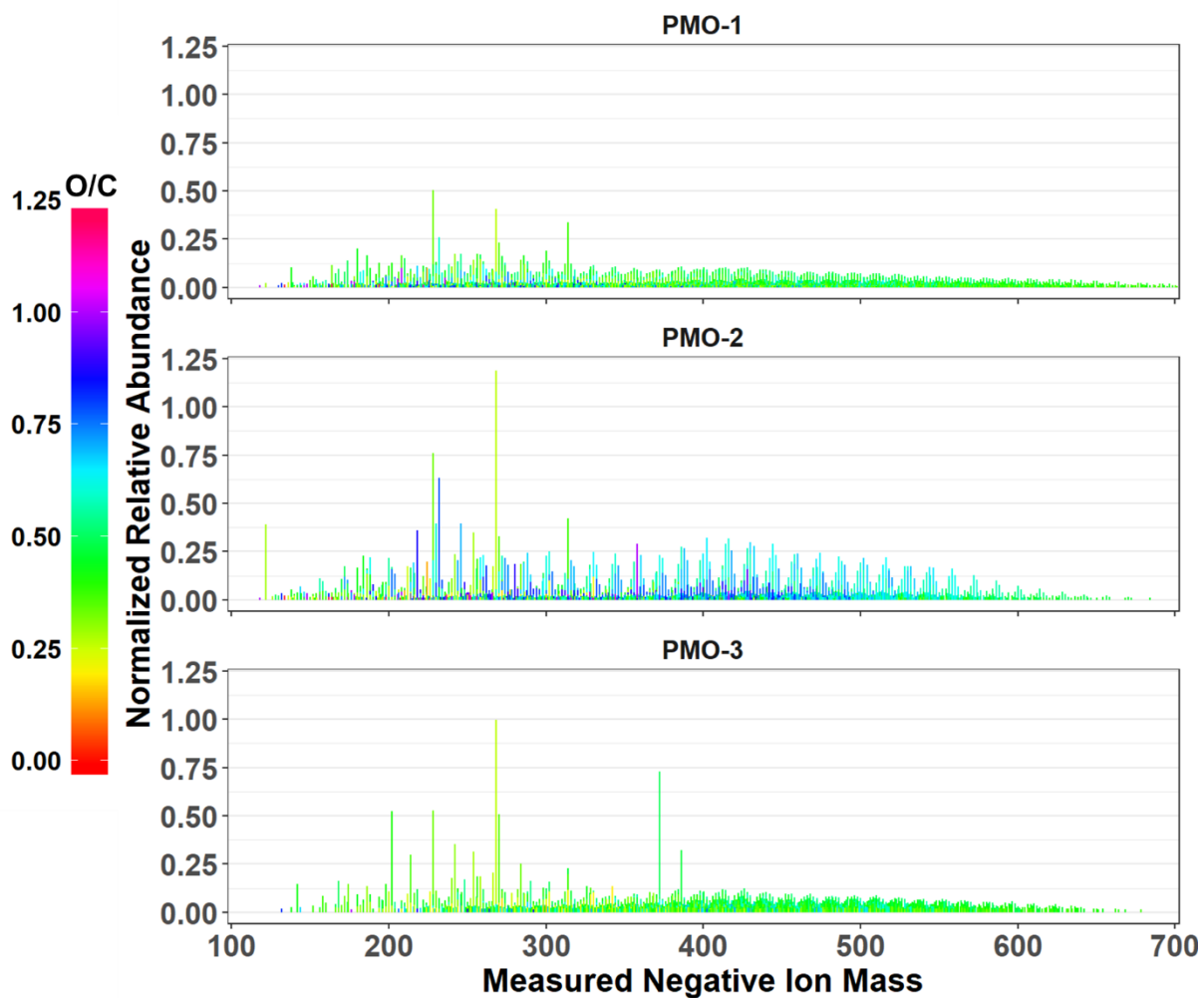


**Figure S6.** Reconstructed mass spectra showing the full abundance of all peaks. This is the same plot as Fig. 2 of the manuscript, just with fully expanded y axis.

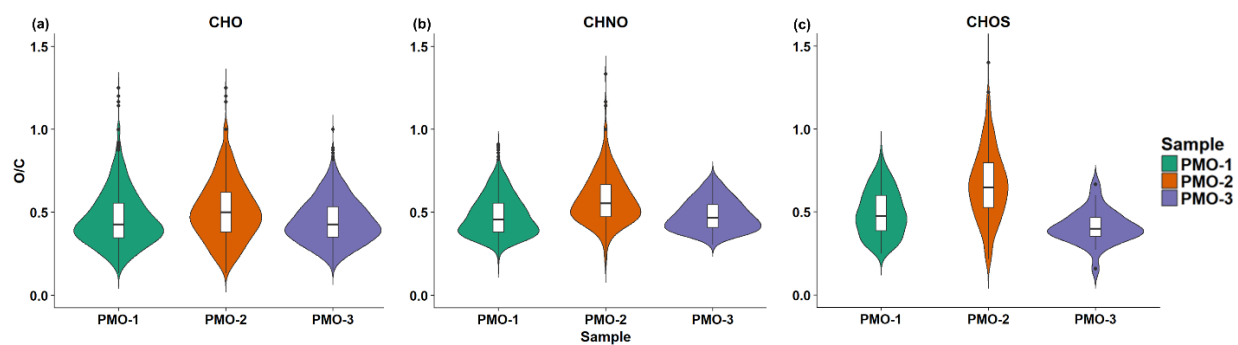


**Figure S7.** Violin plots showing the number distribution of species according to their O/C values separated by molecular groups.

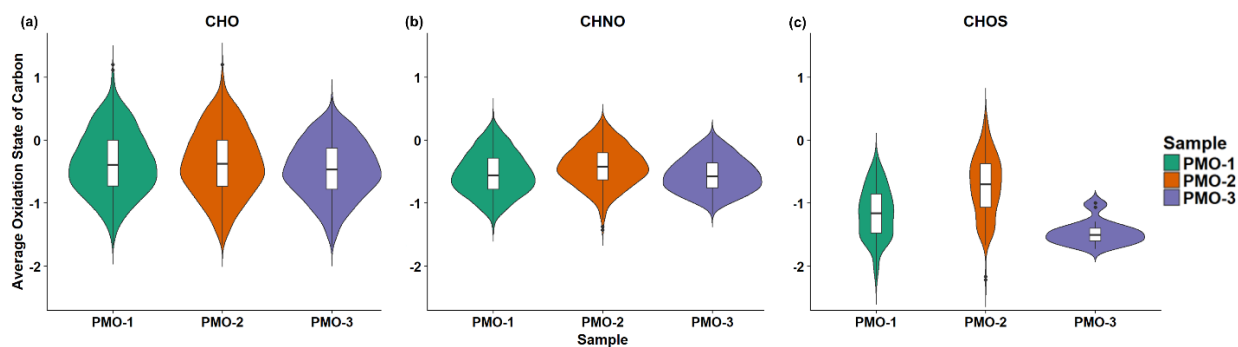


**Figure S8.** Violin plots showing the number distribution of species according to their OS<sub>C</sub> values separated by molecular groups.

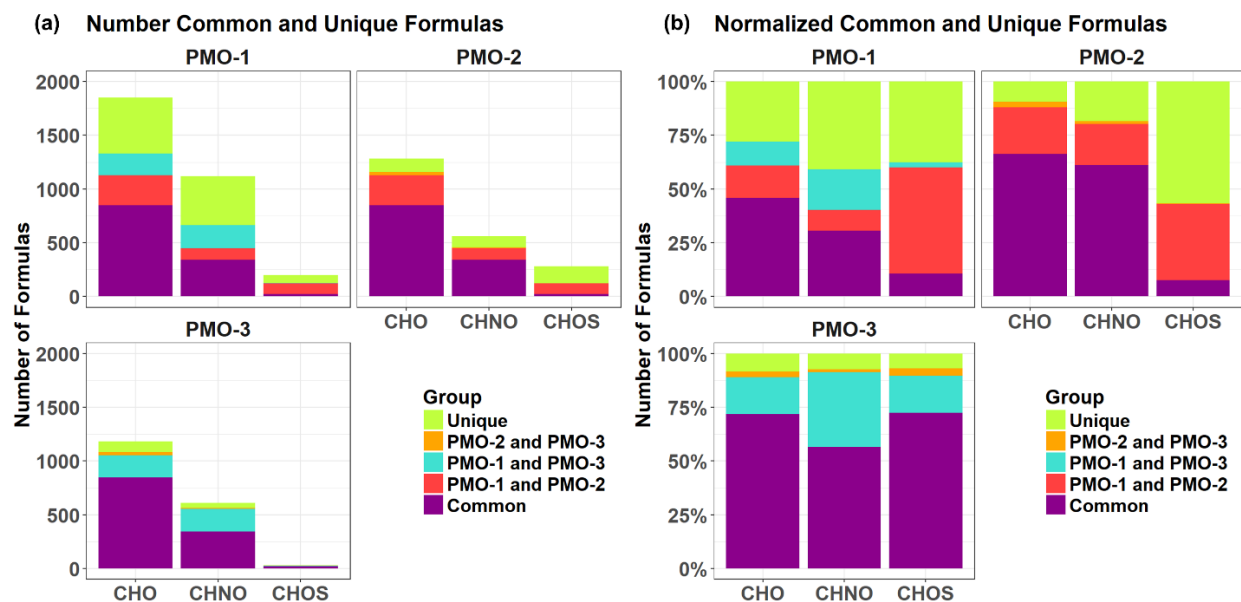


**Figure S9.** Molecular formulas common to all three samples and those unique to each sample presented as the total number of formulas (a) and as a percent of total number of formulas (b).

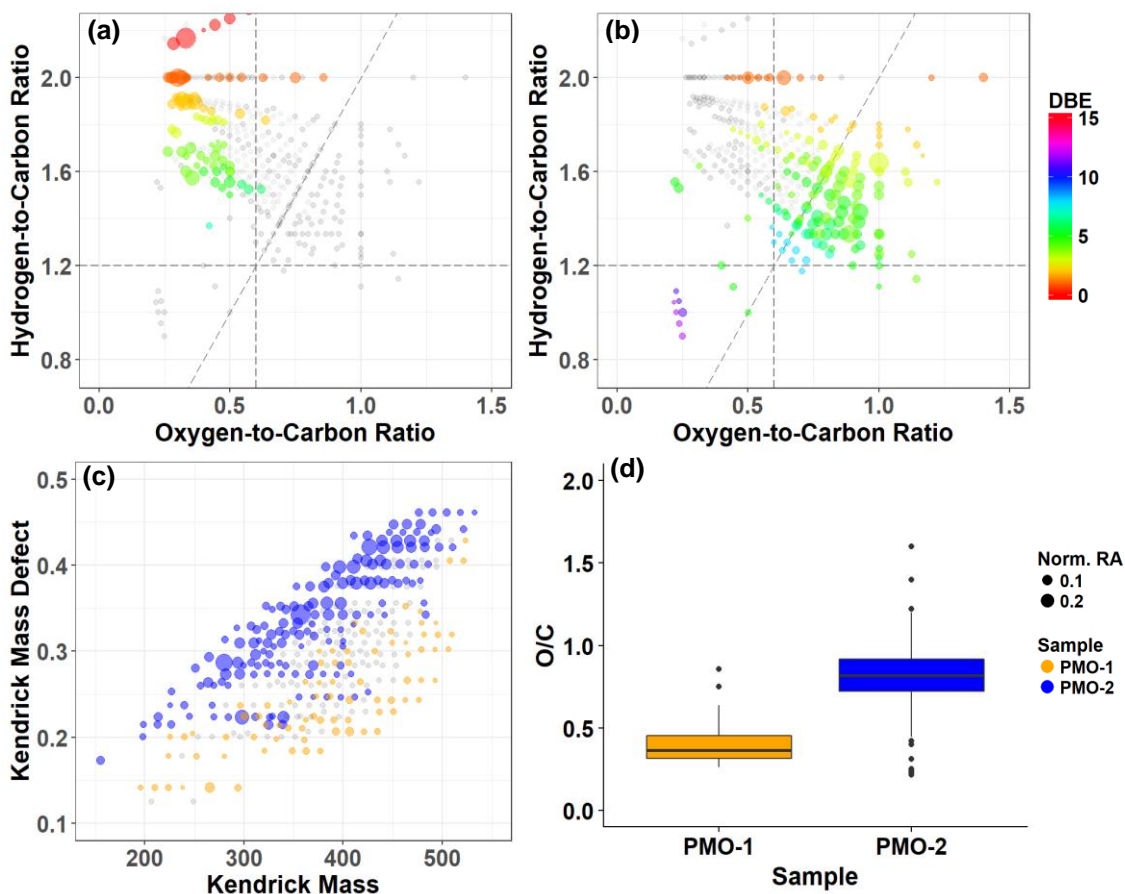


**Figure S10.** A comparison of PMO-1 and PMO-2 CHOS molecular formulas using van Krevelen (a, b), Kendrick plots (c), and O/C box plots (d). Common CHOS molecular formulas (grey) and unique CHOS molecular formulas (colored) are indicated in a-c.

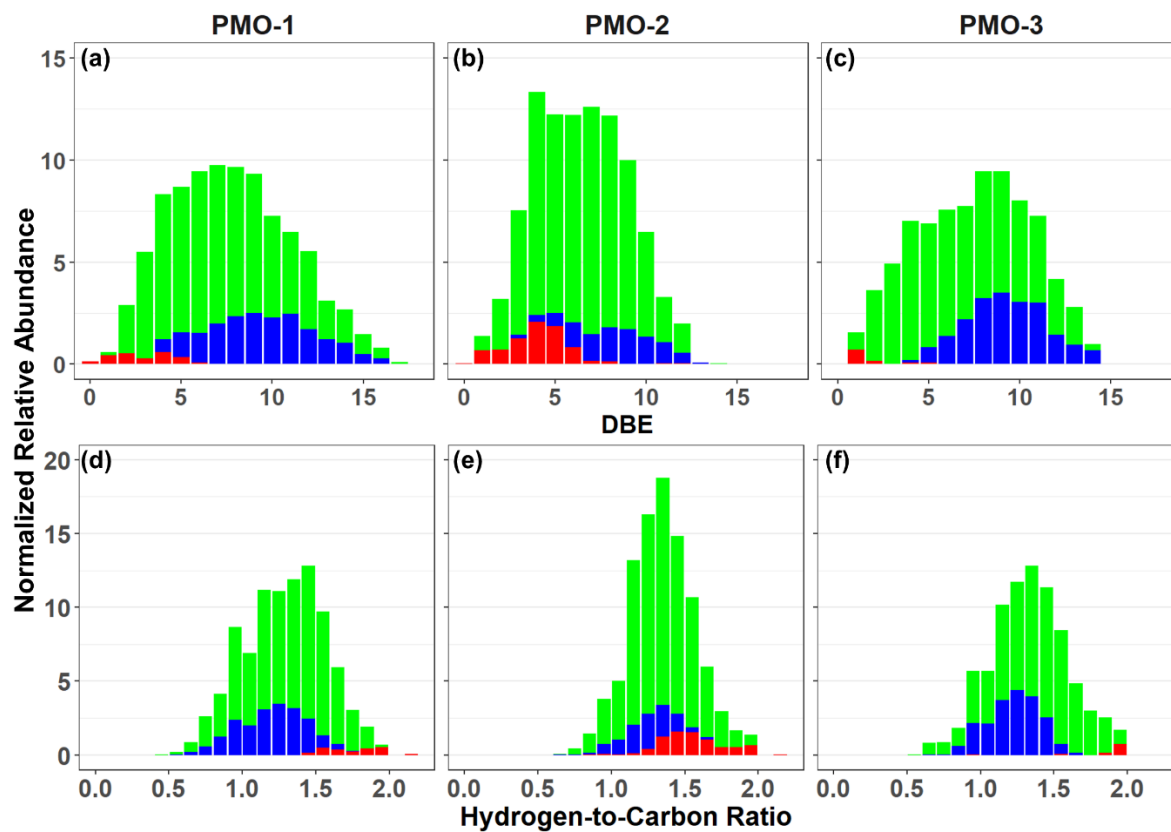
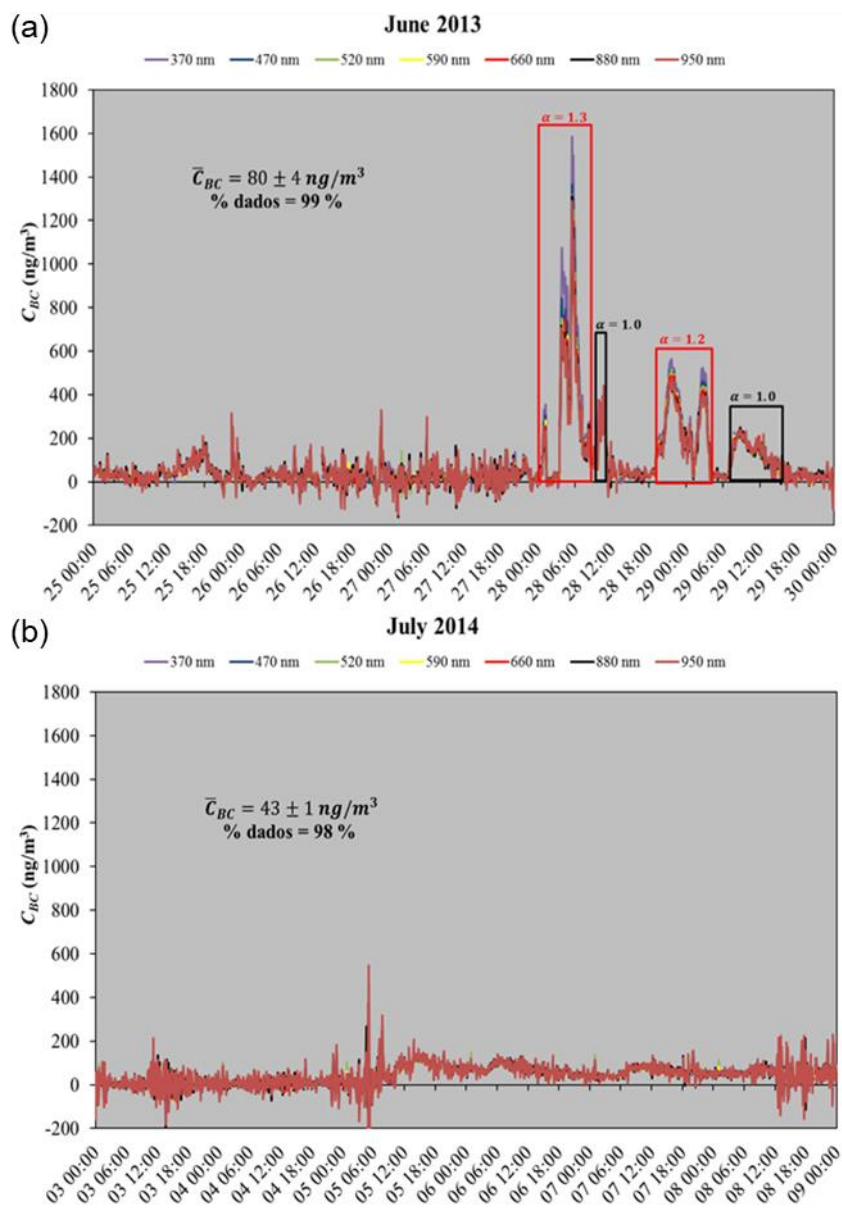
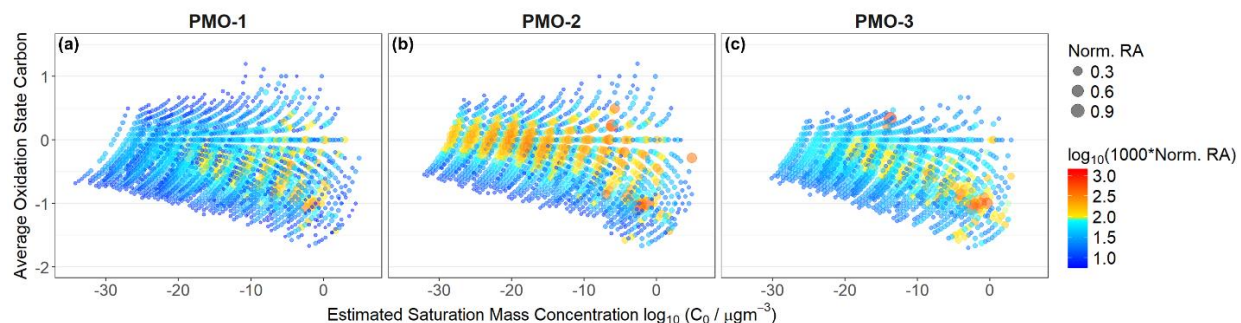


Figure S11. Histograms of the molecular formula DBE (a-c) and H/C (d-f).



**Figure S12.** Aethalometer results for the PMO-1 (a) and PMO-2 (b) sampling periods. A few days before and after each sampling period are included for reference. Note the tallest wavelength dependent peak present from approximately 28 June at 00:00 to 28 June at 09:00 local time (first red box), which corresponds to the sampling period of PMO-1. When the absorption angstrom exponent ( $\alpha$ ) equals 1, it suggests black carbon, when it is  $\geq 1.2$  it suggests presence of brown carbon as well. Due to instrument maintenance/repair no data were available for the time period associated with PMO-3. The sampling period for PMO-2 did not show wavelength dependence.



**Figure S13.**  $OS_C$  vs. volatility plots for the three samples. Volatility estimates were made using the Donahue et al. (2011) method. Only volatility for CHO species can be estimated with this method. Color is the logarithm of the normalized relative abundance multiplied by 1000. Of interest is the increased abundance of low volatility, higher oxidation species in PMO-2 relative to PMO-1 and PMO-3, indicating the importance of these species to this sample and highlighting a difference between these samples.

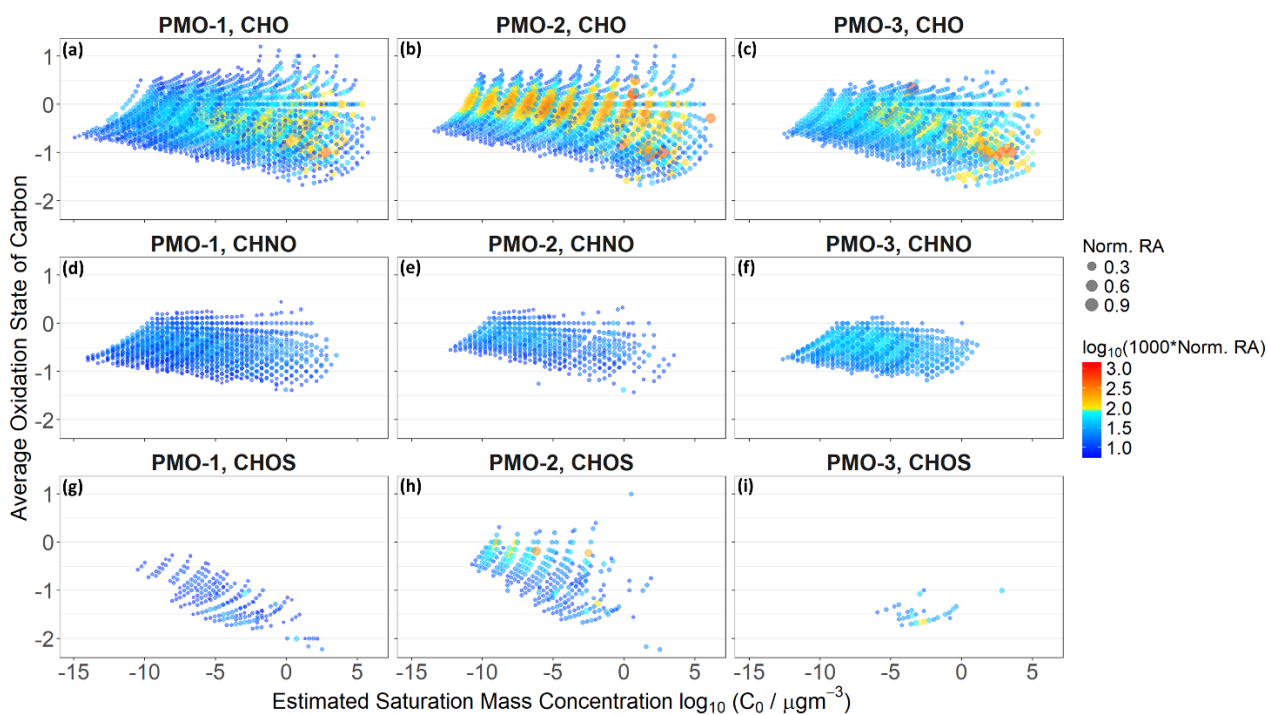


**Figure S14.** Group separated  $OS_C$  vs. volatility plots for the three samples. Volatility estimated using the Li et al. (2016) method. Color is the logarithm of the normalized RA multiplied by 1000. The same increase in abundance for low volatility, higher oxidation species is observed in this figure as in Fig. S13.

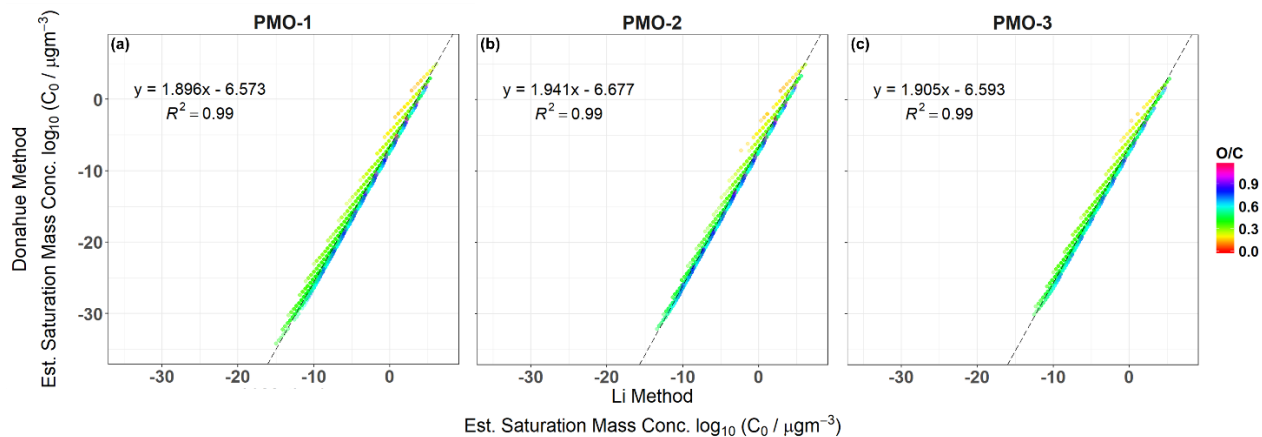


**Figure S15.** Correlation plot of volatility calculated by the Li et al. (2016) method and the Donahue et al. (2011) method. The relation is linear although the slope of the line is nearly two, indicating that the Donahue method predicts values that are roughly two times what the Li method predicts, at least for the low and extremely low volatility species presented here.

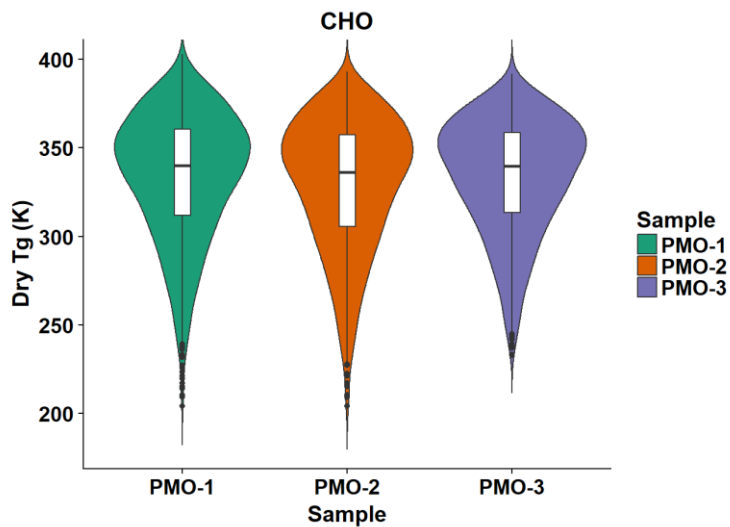


**Figure S16.** Violin plots showing the distribution of dry  $T_g$  values for each sample

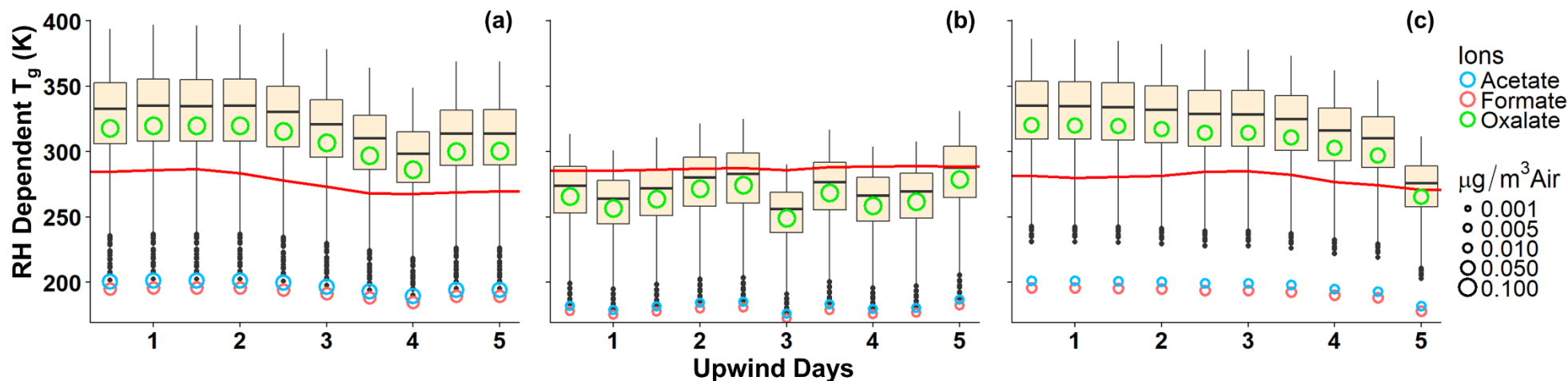


**Figure S17.** Boxplots showing the distributions of the relative humidity dependent  $T_g$  values for each sample over the last five days of transport. The open circles represent the Boyer-Kauzmann estimated  $T_g$  values for the acid forms of the three most abundant low MW organic ions not observed in FT-ICR mass spectra. The symbols are scaled by their ambient concentration. The red line represents the mean ambient temperature from the GFS analysis. The samples PMO-1, PMO-2, and PMO-3 are shown in panels (a), (b), and (c), respectively. The centerline of the boxplot represents the median, the top and bottom of the “box” represent the third and first quartiles, respectively. The “whiskers” represent  $Q3 + 1.5 \times \text{interquartile range (IQR, } Q3-Q1)$  (maximum) and  $Q1 - 1.5 \times \text{(IQR)}$  (minimum).

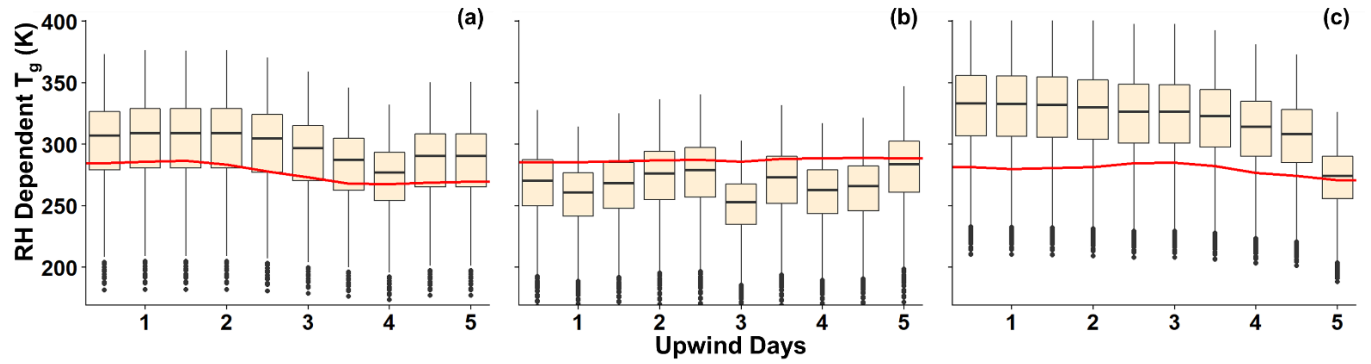


**Figure S18.** Relative humidity dependent  $T_g$  distribution box plots with  $\pm 21$  K uncertainty (DeRieux et al., 2018) applied. Panels (a), (b), and (c) show the distributions for PMO-1, PMO-2, and PMO-3, respectively. Three distributions were calculated for each sample, one with 21 K added to the dry  $T_g$ , one with 21 K subtracted from the dry  $T_g$ , and one with the original  $T_g$  values. The three data sets were combined here. The inclusion of the  $\pm 21$  K uncertainty does not significantly impact the range of observations. The centerline of the boxplot represents the median, the top and bottom of the “box” represent the third and first quartile respectively. The “whiskers” represent  $Q3 + 1.5 \times \text{interquartile range (IQR, } Q3-Q1)$  (maximum) and  $Q1 - 1.5 \times \text{(IQR)}$  (minimum).

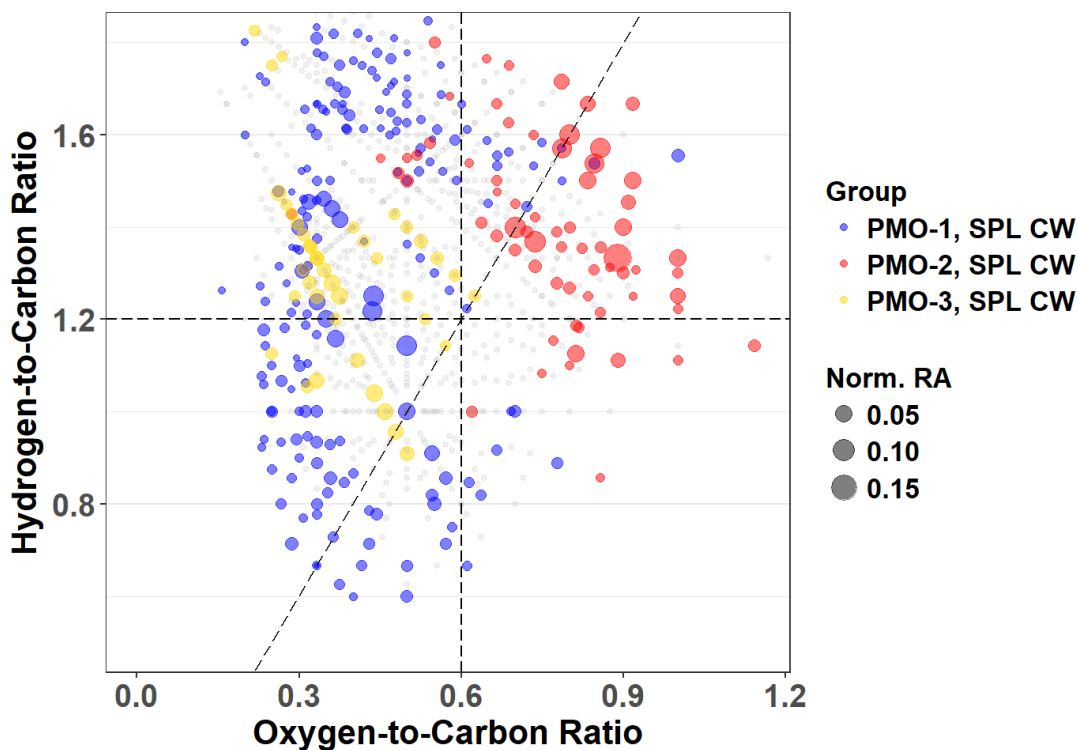


**Figure S19.** Van Krevelen plot showing the molecular formulas that are common to only one PMO sample and the cloud water samples from SPL (Zhao et al., 2014). PMO-2 (red) molecular formulas located nearly exclusively in highly oxidized region of plot, may indicate cloud processing. Common molecular formulas from either PMO-1 (blue) and PMO-3 (gold) may be related to the biomass combustion that influenced the supercooled cloud water collected in the winter at SPL. Formulas that are common to two or more PMO samples and CW are in grey.

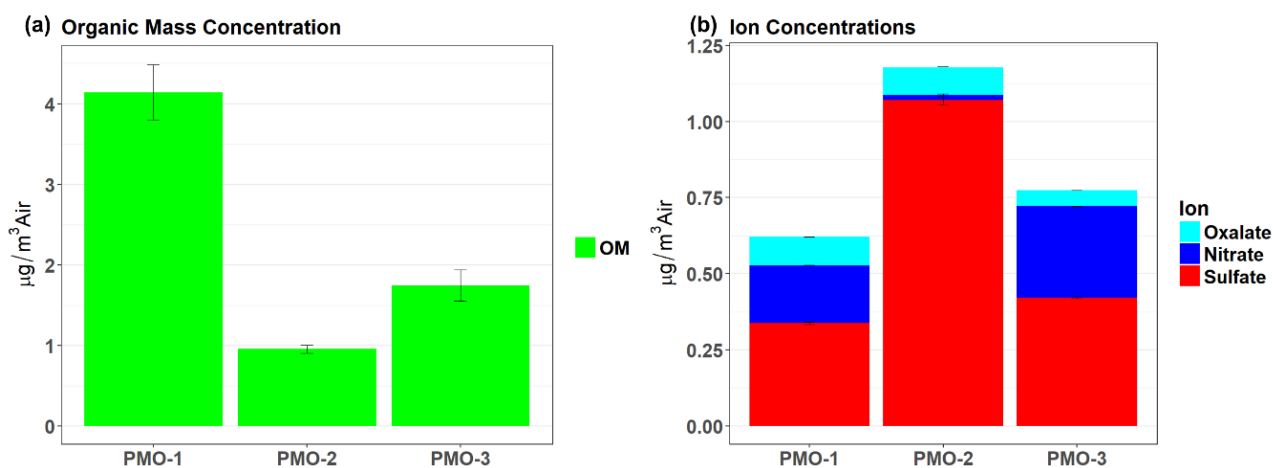


**Figure S20.** Organic mass concentrations (a) and sulfate, nitrate and oxalate concentrations (b).

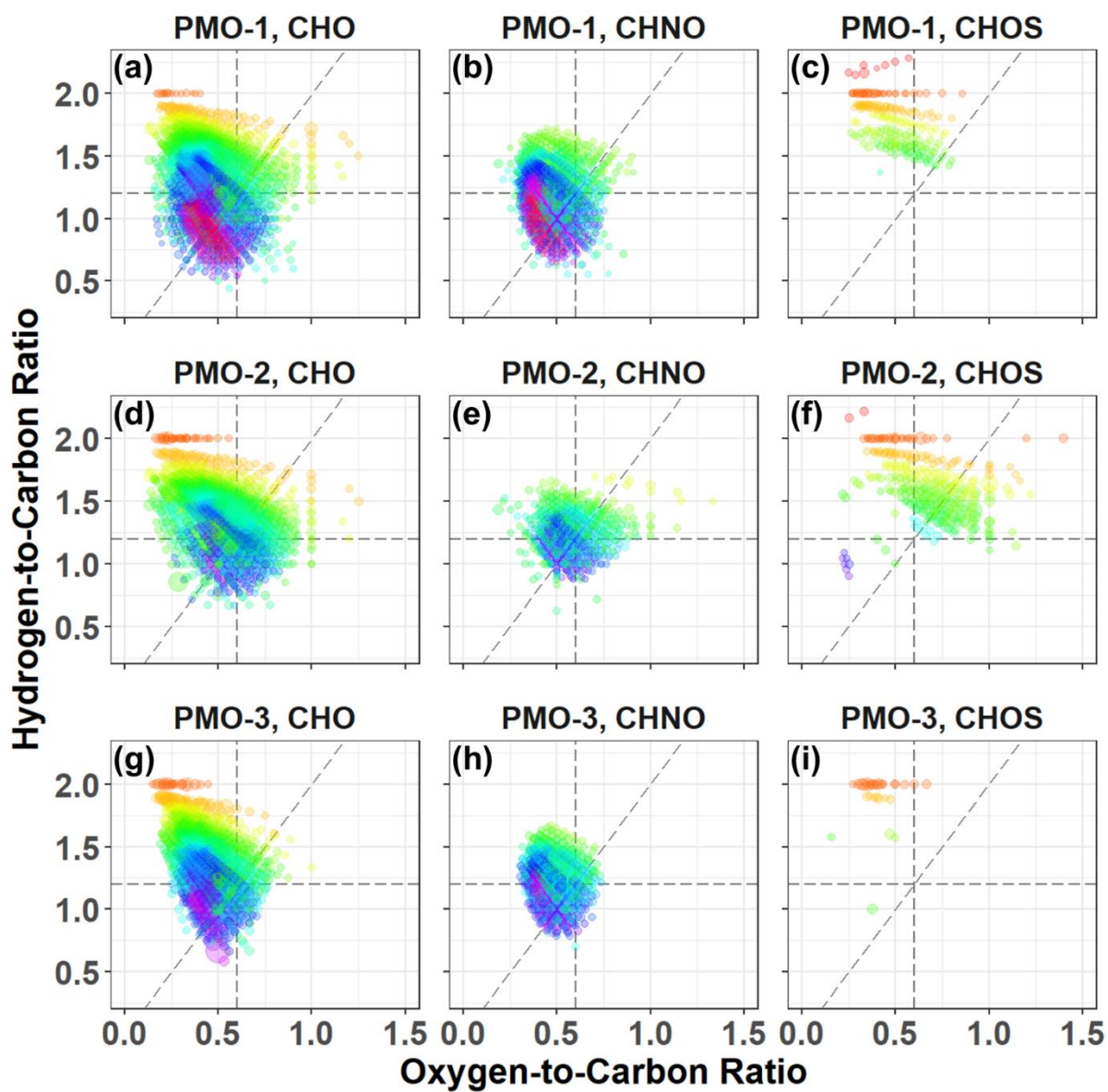


**Figure S21** Group separated van Krevelen diagrams for the three samples. PMO-1 is in panels a-c, PMO-2 in panels d-f, and PMO-3 in panels g-i.

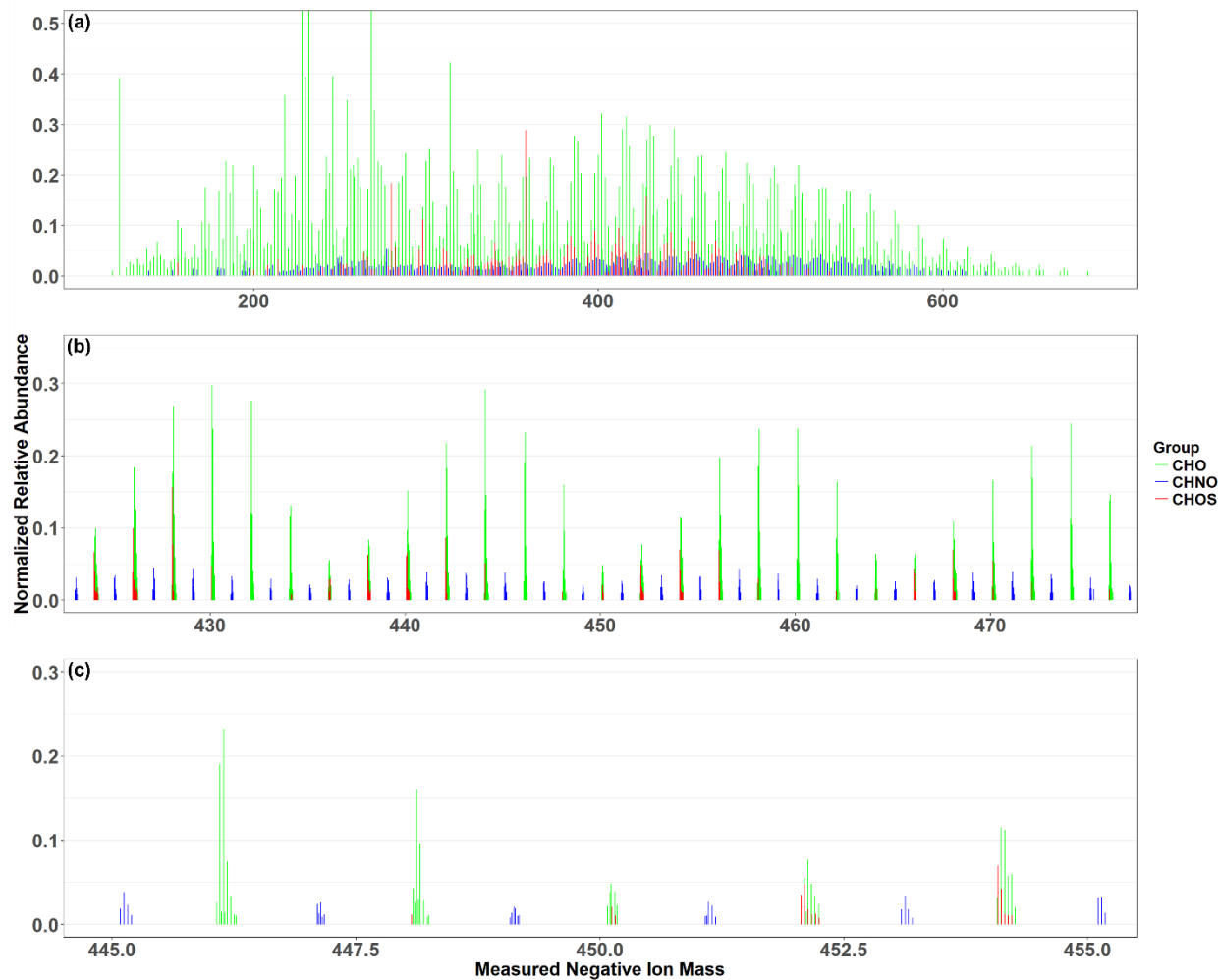


**Figure S22.** Progressively zoomed reconstructed mass spectrum of PMO-2 to demonstrate complexity of the sample.

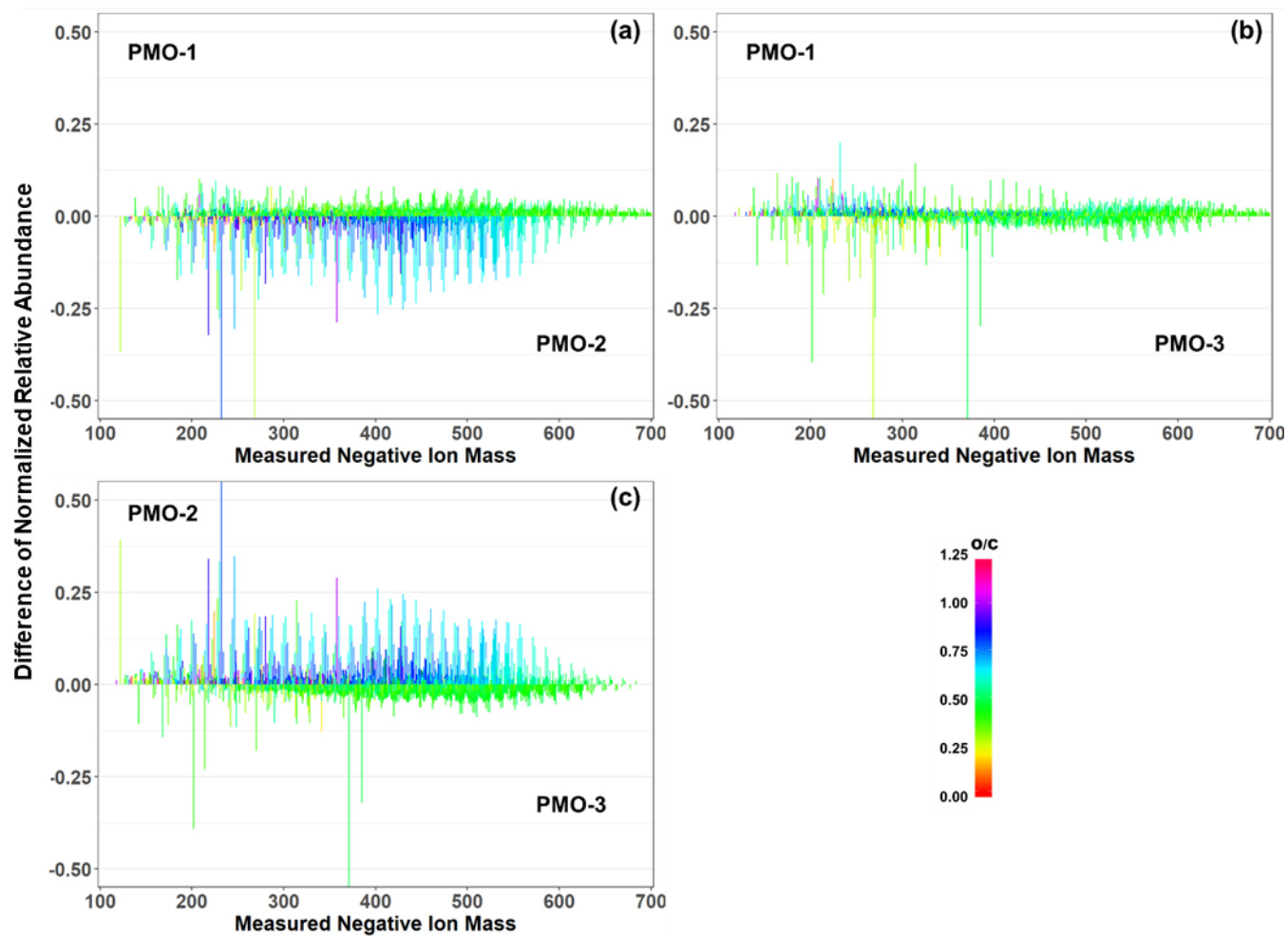


**Figure S23.** Difference mass spectra comparing the three PMO samples. The species more abundant in one sample or another are elevated in the correspondingly labeled half of the plot. PMO-1 vs. PMO-2 (a), PMO-1 vs. PMO-3 (b), and PMO-2 vs. PMO-3 (c).

## Supplemental Equations

**Equation S1.** The average oxidation state of carbon ( $OS_C$ ) from Kroll et al. (2011). Sulfur and nitrogen play a role in the oxidation of the species, which varies based on their oxidation state. In this case, sulfur and nitrogen are assumed to be fully oxidized.

$$OS_C \approx 2 * \frac{\#O}{\#C} - \frac{\#H}{\#C} - 5 * \frac{\#N}{\#C} - 6 * \frac{\#S}{\#C}$$

**Equation S2.** The aromaticity index (AI) from Koch and Dittmar (2006; 2016). This is the most conservative method for calculating aromaticity as it assumes that all oxygen is in carbonyl groups. The threshold for olefinic species is  $0 < AI \leq 0.5$ , for aromatic it is  $0.5 < AI \leq 0.67$ , and for condensed aromatic it is  $0.67 < AI \approx 1$ . All other species are defined as  $AI = 0$  making them aliphatic.

$$AI = \frac{1 + C - O - S - 0.5 * H - 0.5 * N}{C - O - S - N}$$

**Equation S3.** The modified aromaticity index ( $AI_{mod}$ ) from Koch and Dittmar (2006; 2016). Here it is assumed that half of the oxygen is in carbonyl groups. The threshold for olefinic species is  $0 < AI_{mod} \leq 0.5$ , for aromatic it is  $0.5 < AI_{mod} \leq 0.67$ , and for condensed aromatic it is  $0.67 < AI_{mod} \approx 1$ . All other species are defined as  $AI_{mod} = 0$  making them aliphatic

$$AI_{mod} = \frac{1 + C - 0.5 * O - S - 0.5 * H - 0.5 * N}{C - 0.5 * O - S - N}$$

**Equation S4.** The number of double bond (and rings) equivalents (DBE). C represents carbon, H represents hydrogen, X represents halogens, and N represents nitrogen. Elements with 2 covalent bonds (oxygen and sulfur) are cancelled out in this equation.

$$DBE = \#C + 1 - \frac{\#H}{2} - \frac{\#X}{2} + \frac{\#N}{2}$$

**Equation S5.** Estimation of the glass transition temperature from DeRieux et al., 2018.  $n_C^0$  is the carbon reference number ( $12.13 \pm 2.66$ ),  $b_C$ ,  $b_H$ , and  $b_O$  are the contributions of each atom to  $T_g$ , and  $b_{CH}$  and  $b_{CO}$  represent the contribution of carbon-hydrogen and carbon-oxygen bonds respectively. Values for the terms can be found in DeRieux et al. 2018. This equation determines the dry glass transition temperature. The Gordon-Taylor Equation (Eq. S6) is required to convert the glass transition temperature for non-dry conditions.

$$T_g = (n_C^0 + \ln(n_C)) b_C + \ln(n_H) b_H + \ln(n_C) \ln(n_H) b_{CH} + \ln(n_O) b_O + \ln(n_C) \ln(n_O) b_{CO}$$

**Equation S6.** Gordon-Taylor Equation from DeRieux et al. (2018). This is used to calculate the glass transition temperature in humid conditions.  $w_{org}$  is the mass fraction of organics,  $T_{g,w}$  is the glass transition temperature for water (136 K),  $k_{GT}$  is the Gordon-Taylor constant (assumed to be 2.5, consistent with DeRieux et al., 2018 and Shiraiwa et al., 2017), and  $T_{g,org}$  is the dry glass transition temperature calculated by Eq. S5. For more detail see DeRieux et al., 2018 and Shiraiwa et al., 2017.

$$T_g(w_{org}) = \frac{(1 - w_{org})T_{g,w} + \frac{1}{k_{GT}}w_{org}T_{g,org}}{(1 - w_{org}) + \frac{1}{k_{GT}}w_{org}}$$

**Equation S7.** Adapted Gordon-Taylor equation with inputs for relative humidity (RH), dry glass transition temperature, and ambient temperature. This generates the phase state ratio (PSR), which predicts the phase the molecular species is likely in,  $PSR \geq 1$  is solid,  $0.8 \leq PSR < 1$  is semi-solid, and  $PSR < 0.8$  is liquid. This equation converts  $w_{org}$  to a relative humidity dependent term as described in DeRieux et al. (2018) and Shiraiwa et al. (2017), and converts  $1/k_{GT}$  to 0.4, which is its value using the assumption of  $k_{GT}$  equals 2.5.  $T_{amb}$  is the ambient temperature. The relative humidity dependent  $T_g$  is calculated using the calculation in the numerator.

$$\text{Phase State Ratio} = \frac{\left( \left( 1 - \frac{1.4 - \frac{1.4 * RH}{100}}{1.4 - \frac{1.28 * RH}{100}} \right) * 136 + 0.4 * \left( \frac{1.4 - \frac{1.4 * RH}{100}}{1.4 - \frac{1.28 * RH}{100}} \right) * T_{g,org} \right)}{\left( \left( 1 - \frac{1.4 - \frac{1.4 * RH}{100}}{1.4 - \frac{1.28 * RH}{100}} \right) + 0.4 * \left( \frac{1.4 - \frac{1.4 * RH}{100}}{1.4 - \frac{1.28 * RH}{100}} \right) \right)} T_{amb}$$

## References

- Bougiatioti, A., Stavroulas, I., Kostenidou, E., Zarnpas, P., Theodosi, C., Kouvarakis, G., Canonaco, F., Prevot, A. S. H., Nenes, A., Pandis, S. N. and Mihalopoulos, N.: Processing of biomass-burning aerosol in the eastern Mediterranean during summertime, *Atmos. Chem. Phys.*, 14(9), 4793–4807, doi:10.5194/acp-14-4793-2014, 2014.
- Chang, O., Procedure for the analysis of particulate anions and cations in motor vehicle exhaust by ion chromatography, California EPA Air Resources Board, 2011.
- Cook, R. D., Lin, Y.-H., Peng, Z., Boone, E., Chu, R. K., Dukett, J. E., Gunsch, M. J., Zhang, W., Tolic, N., Laskin, A. and Pratt, K. A.: Biogenic, urban, and wildfire influences on the molecular composition of dissolved organic compounds in cloud water, *Atmos. Chem. Phys.*, 17(24), 15167–15180, doi:10.5194/acp-17-15167-2017, 2017.
- DeRieux, W.-S. W., Li, Y., Lin, P., Laskin, J., Laskin, A., Bertram, A. K., Nizkorodov, S. A. and Shiraiwa, M.: Predicting the glass transition temperature and viscosity of secondary organic material using molecular composition, *Atmos. Chem. Phys.*, 18(9), 6331–6351, doi:10.5194/acp-18-6331-2018, 2018.
- Donahue, N., Epstein, S., Pandis, S. and Robinson, A.: A two-dimensional volatility basis set: 1. organic-aerosol mixing thermodynamics, *Atmos. Chem. Phys.*, 11(7), 3303–3318, doi:10.5194/acp-11-3303-2011, 2011.
- Dzepina, K., Mazzoleni, C., Fialho, P., China, S., Zhang, B., Owen, R. C., Helmig, D., Hueber, J., Kumar, S., Perlinger, J. A., Kramer, L. J., Dziobak, M. P., Ampadu, M. T., Olsen, S., Wuebbles, D. J., and Mazzoleni, L. R.: Molecular characterization of free tropospheric aerosol collected at the Pico Mountain Observatory: a case study with a long-range transported biomass burning plume, *Atmos. Chem. Phys.*, 15(9), 5047–5068, doi:10.5194/acp-15-5047-2015, 2015.
- El-Zanan, H. S., Lowenthal, D. H., Zielinska, B., Chow, J. C. and Kumar, N.: Determination of the organic aerosol mass to organic carbon ratio in IMPROVE samples, *Chemosphere*, 60(4), 485–496, doi:10.1016/j.chemosphere.2005.01.005, 2005.
- Honrath, R. E., Helmig, D., Owen, R. C., Parrish, D. D. and Tanner, D. M.: Nonmethane hydrocarbons at Pico Mountain, Azores: 2. Event-specific analyses of the impacts of mixing and photochemistry on hydrocarbon ratios, *J. Geophys. Res – Atmos.*, 113(D20), doi:10.1029/2008jd009832, 2008.
- Iinuma, Y., Boege, O., Graefe, R., and Herrmann, H.: Methyl-Nitrocatechols: Atmospheric Tracer Compounds for Biomass Burning Secondary Organic Aerosols, *Environ. Sci. Technol.*, 44, 8453–8459, doi:10.1021/es102938a, 2010.
- Kleissl, J., Honrath, R. E., Dziobak, M. P., Tanner, D., Val Martín, M., Owen, R. C. and Helmig, D.: Occurrence of upslope flows at the Pico mountaintop observatory: A case study of orographic flows on a small, volcanic island, *J. Geophys. Res-Atmos.*, 112(D10), doi:10.1029/2006jd007565, 2007.
- Koch, B. P. and Dittmar, T.: From mass to structure: an aromaticity index for high-resolution mass data of natural organic matter, *Rapid Commun. Mass Sp.*, 20(5), 926–932, doi:10.1002/rcm.2386, 2006.
- Koch, B. P. and Dittmar, T.: From mass to structure: an aromaticity index for high-resolution mass data of natural organic matter, *Rapid Commun. Mass Sp.*, 30(1), 250, doi: 10.1002/rcm.7433, 2016.
- Kroll, J. H., Donahue, N. M., Jimenez, J. L., Kessler, S. H., Canagaratna, M. R., Wilson, K. R., Altieri, K. E., Mazzoleni, L. R., Wozniak, A. S., Bluhm, H., Mysak, E. R., Smith, J. D., Kolb, C. E. and Worsnop, D. R.: Carbon oxidation state as a metric for describing the chemistry of atmospheric organic aerosol, *Nat. Chem.*, 3(2), nchem.948, doi:10.1038/nchem.948, 2011.
- Li, Y., Pöschl, U. and Shiraiwa, M.: Molecular corridors and parameterizations of volatility in the chemical evolution of organic aerosols, *Atmos. Chem. Phys.*, 16(5), 3327–3344, doi:10.5194/acp-16-3327-2016, 2016.
- Lin, P., Aiona, P. K., Li, Y., Shiraiwa, M., Laskin, J., Nizkorodov, S. A., and Laskin, A.: Molecular Characterization of Brown Carbon in Biomass Burning Aerosol Particles, *Environ. Sci. Technol.*, 50, 11815–11824, doi:10.1021/acs.est.6603024, 2016.
- Mazzoleni, L. R., Ehrmann, B. M., Shen, X., Marshall, A. G. and Collett, J. L.: Water-Soluble Atmospheric Organic Matter in Fog: Exact Masses and Chemical Formula Identification by Ultrahigh-Resolution Fourier Transform Ion Cyclotron Resonance Mass Spectrometry, *Environ. Sci. Technol.*, 44(10), 3690–3697, doi:10.1021/es903409k, 2010.
- Mazzoleni, L. R., Saranjampour, P., Dalbec, M. M., Samburova, V., Hallar, A. G., Zielinska, B., Lowenthal, D. H. and Kohl, S.: Identification of water-soluble organic carbon in non-urban aerosols using ultrahigh-

- resolution FT-ICR mass spectrometry: organic anions, *Environ. Chem.*, 9(3), 285–297, doi:10.1071/en11167, 2012.
- Olivier, J.G.J. and Berdowski, J.J.M.: Global emissions sources and sinks, in: *The Climate System*, Berdowski, J., Guicherit, R. and Heij, B.J., A.A. Balkema Publishers/Swets & Zeitlinger Publishers, Lisse, The Netherlands. 33-78, 2001.
- Owen, R. C. and Honrath, R. E.: Technical note: a new method for the Lagrangian tracking of pollution plumes from source to receptor using gridded model output, *Atmospheric Chemistry and Physics*, 9(7), 2577–2595, doi:10.5194/acp-9-2577-2009, 2009.
- Putman, A. L., Offenberg, J. H., Fisseha, R., Kundu, S., Rahn, T. A. and Mazzoleni, L. R.: Ultrahigh-resolution FT-ICR mass spectrometry characterization of  $\alpha$ -pinene ozonolysis SOA, *Atmos. Env.*, 46, 164–172, doi:10.1016/j.atmosenv.2011.10.003, 2012.
- Rémillard, J., Kollias, P., Luke, E. and Wood, R.: Marine Boundary Layer Cloud Observations in the Azores, *J. Climate*, 25(21), 7381–7398, doi:10.1175/jcli-d-11-00610.1, 2012.
- Samburova, B., Hallar, A. G., Mazzoleni, L. R., Saranjampour, P., Lowenthal, D., Kohl, S. D., Zielinska, B.: Composition of water-soluble organic carbon in non-urban atmospheric aerosol collected at the Storm Peak Laboratory. *Environ. Chem.*, 10(5), 370-380, <https://doi.org/10.1071/EN13079>, 2013.
- Seibert, P. and Frank, A.: Source-receptor matrix calculation with a Lagrangian particle dispersion model in backward mode, *Atmospheric Chemistry and Physics*, 4(1), 51–63, doi:10.5194/acp-4-51-2004, 2004.
- Shiraiwa, M., Li, Y., Tsimpidi, A., Karydis, V., Berkemeier, T., Pandis, S., Lelieveld, J., Koop, T. and Pöschl, U.: Global distribution of particle phase state in atmospheric secondary organic aerosols, *Nat. Commun.*, 8, ncomms15002, doi:10.1038/ncomms15002, 2017.
- Stohl, A., Forster, C., Frank, A., Seibert, P. and Wotawa, G.: Technical note: The Lagrangian particle dispersion model FLEXPART version 6.2, *Atmospheric Chemistry and Physics*, 5(9), 2461–2474, doi:10.5194/acp-5-2461-2005, 2005.
- Zhang, B., Owen, R. C., Perlinger, J. A., Helmig, D., Val Martín, M., Kramer, L., Mazzoleni, L. R. and Mazzoleni, C.: Ten-year chemical signatures associated with long-range transport observed in the free troposphere over the central North Atlantic, *Elem. Sci. Anth.*, 5, doi:10.1525/elementa.194, 2017.
- Zhao, Y., Hallar, A. G. and Mazzoleni, L. R.: Atmospheric organic matter in clouds: exact masses and molecular formula identification using ultrahigh-resolution FT-ICR mass spectrometry, *Atmos. Chem. Phys.*, 13(24), 12343–12362, doi:10.5194/acp-13-12343-2013, 2013.